Whole-body Magnetic Resonance Imaging at 0.05 Tesla

Yujiao Zhao[1,2], Ye Ding[1,2], Vick Lau[1,2], Christopher Man[1,2], Shi Su[1,2], Linfang Xiao[1,2], Alex T. L. Leong[1,2], Ed X. Wu[1,2*]

[1]Laboratory of Biomedical Imaging and Signal Processing, The University of Hong Kong, Pokfulam, Hong Kong SAR, China

[2]Department of Electrical and Electronic Engineering, The University of Hong Kong, Pokfulam, Hong Kong SAR, China

[*]Correspondence should be addressed to Professor Ed X. Wu, Ph.D.:
Department of Electrical and Electronic Engineering, The University of Hong Kong, Pokfulam, Hong Kong, Hong Kong SAR, China
Fax: +852-2859-8738
Tel: +852-3917-7096
Email: ewu@eee.hku.hk

Zhao Y, Ding Y, Lau V, Man C, Su S, Xiao L, Leong ATL, Wu EX. Whole-body magnetic resonance imaging at 0.05 Tesla. Science. 2024 May 10;384(6696):eadm7168. doi: 10.1126/science.adm7168.

Abstract

Despite a half-century of advancements, global MRI accessibility remains limited and uneven, hindering its full potential in healthcare. Initially, MRI development focused on low fields around 0.05 Tesla, but progress halted after the introduction of the 1.5 Tesla whole-body superconducting scanner in 1983. Using a permanent 0.05 Tesla magnet and deep learning for electromagnetic interference elimination, we developed a whole-body scanner that operates using a standard AC wall power outlet and without radiofrequency and magnetic shielding. We demonstrated its wide-ranging applicability for imaging various anatomical structures. Furthermore, we developed 3D deep learning reconstruction to boost image quality by harnessing extensive high-field MRI data. These advances pave the way for affordable deep learning-powered ultra-low-field MRI scanners, addressing unmet clinical needs in diverse healthcare settings worldwide.

Introduction

The seminal development of magnetic resonance imaging (MRI) by Paul C. Lauterbur and Sir Peter Mansfield five decades ago revolutionized modern medicine (*1, 2*). MRI is now widely regarded as one of the most important inventions for healthcare (*3*). Over 150 million MRI examinations are performed worldwide each year (*4*), with applications ranging from diagnosing and prognosing diseases such as tumors and strokes, to evaluating injuries in the nervous, hepatobiliary, pancreatic, and musculoskeletal systems, and to guidance of interventional procedures. MRI holds inherent advantages over other imaging modalities, specifically, it is non-ionizing, non-invasive, inherently three-dimensional, quantitative, and multi-parametric (*5*). These qualities not only make MRI superior to other imaging modalities but also position it as a promising platform for future artificial intelligence-driven medical diagnoses.

Nonetheless, MRI accessibility remains low and highly uneven worldwide. As per the 2022 Organisation for Economic Co-operation and Development (OECD) statistics, there are around 70,000 MRI scanner installations across the globe (*6*). The distribution of these scanners is primarily concentrated in developed nations, with limited availability in low and middle-income countries. For instance, Africa has a mere 0.7 MRI scanners per million residents (*7*), in stark contrast to the United States and Japan, which have 40 and 55 scanners per million inhabitants, respectively, presenting an exemplary case of ever-expanding global healthcare disparity (*8*). This scenario primarily stems from the considerable costs associated with the procurement, installation, maintenance, and operation of existing standard high-field superconducting MRI scanners (1.5 T and 3 T). These clinical MRI scanners are predominantly located in highly specialized radiology departments, large centralized imaging centers, and often situated on the ground floors of hospitals and clinics and with magnetic shielding. As a result, MRI scanners are mostly unavailable in trauma centers, acute care facilities, surgery suites, pediatric clinics, and community clinics even in developed countries. Moreover, these scanners prevent external electromagnetic interference (EMI) through the passive use of bulky and fully enclosed radiofrequency (RF) shielded rooms,

thus posing further hardware costs and compromising their mobility and patient-friendliness.

Recently, there have been intensive efforts to develop low-cost MRI scanners for brain imaging at ultra-low-field (ULF) strengths (<0.1 T) (*9-14*). Studies have shown that key neuroimaging protocols can be successfully implemented on ULF scanners, providing valuable information for diagnosing brain lesions like tumor and stroke (*12, 15, 16*). The need for RF shielded rooms is also being challenged by active detection and retrospective removal of environmental EMI signals using analytical and deep learning approaches (*12, 17, 18*), offering the promise of shielding-free, thus portable and more patient-friendly MRI. Recent studies have highlighted the potential of such brain ULF scanners for point-of-care applications in intensive care units and COVID-19 wards (*15, 16, 19*). Concurrently, deep learning advances offer exceptional capabilities for multi-dimensional feature extraction (*20, 21*), presenting approaches to address the low magnetic resonance (MR) signal-to-noise ratio (SNR) inherent to ULF. For example, deep learning superresolution strategies have been recently pursued for brain ULF MRI to suppress image noise and boost resolution by leveraging the homogeneous brain structures and image contrasts available in human brain high-field MRI data (*22, 23*). However, these developments have been confined to the imaging of the brain (*9-14*) and extremities (*24*). To fully harness the potential of ULF MRI for accessible healthcare, it is imperative to develop ULF MRI technologies, including deep learning techniques, for imaging all organs at the whole-body level.

In this study, we present the development of a low-cost, low-power, and computing-driven shielding-free ULF MRI scanner for whole-body imaging. It features a homogeneous 0.05 T permanent magnet and linear imaging gradients, enabling us to implement ULF MRI protocols by building upon the methodologies developed for high-field MRI over the past five decades. To achieve robust EMI elimination for shielding-free scanning, we deployed a method to directly predict EMI-free MR signals via deep learning (*25*). We demonstrated the wide-ranging applicability of this scanner for imaging various anatomical structures, including brain, spine, abdomen, lung, extremity, and heart. Furthermore, we demonstrated the promise of deep learning

3D image formation on this whole-body ULF MRI platform by learning from large-scale high-field MRI data, using a method we developed (*26*).

Results

Shielding-free 0.05 Tesla whole-body MRI scanner design

We demonstrated the feasibility of a cost-effective MRI technology by designing and prototyping a whole-body MRI scanner that operates on a standard AC wall power outlet (single-phase 220V 20A) without any RF or magnetic shielding cages (**Fig. 1**). The system utilized a compact 0.05 T permanent neodymium ferrite boron (NdFeB) magnet with a double-plate structure (**Fig. 1A**). Key magnet components included yokes, NdFeB plates, poles, anti-eddy current plates, and shimming rings (**Fig. 1B**). It generated a 0.05 T field with inhomogeneity <10,000 ppm peak-to-peak over an oblate ellipsoid volume of diameter 40 cm and height 38 cm. After passive shimming, this inhomogeneity was reduced to <200 ppm peak-to-peak. The 5 Gauss fringe field was small, within 104 cm, 114 cm, and 104 cm in X, Y, and Z directions from magnet center. Here, we used standard and low-cost off-the-shelf electronics for simplicity, including console and gradient amplifier. For quantity production, we estimate its hardware material costs to be ~USD 22K mainly for the magnet, gradient and RF, and console subsystems (**Table S1**).

The scanner required no RF shielding cages. To robustly address the EMI from both external environments and internal low-cost electronics during scanning, we deployed active sensing and deep learning to directly predict EMI-free MR signals. Ten small EMI sensing coils were positioned around the scanner and inside the electronic cabinet to simultaneously acquire radiative EMI signals during scanning (**Fig. 1A**). We developed and implemented a method termed deep learning direct signal prediction (Deep-DSP) (*25*) (**Fig. 1C** and **Fig. S1**). In brief, both the MRI receive coil and EMI sensing coils sampled data within two windows - one for MR signal acquisition and the other for EMI signal characterization data acquisition. No MR signal was

present during EMI signal characterization window. Using the synthetic EMI-contaminated MRI data and EMI sensing coil data acquired during the EMI signal characterization window, a residual U-Net model was trained to predict EMI-free MR signal from signals acquired by both types of coils. The trained model was then used to predict EMI-free MR signal from data acquired during the MR signal acquisition window. This Deep-DSP strategy has been shown to yield superior performance (*25*) compared to all existing EMI reduction methods recently developed for brain ULF MRI (*12, 17, 18*). It is worth noting that, in practice, the EMI signal characterization window is not an absolute requirement for Deep-DSP (*25*).

Whole-body imaging at 0.05 Tesla

Over the past few decades, extensive research in high-field superconducting MRI has resulted in the development of a wide range of MRI contrasts and clinical protocols that enable the investigation of various organ structures and physiological abnormalities associated with different pathologies (*27*). The commonly used MRI protocols are predominately based on the T1-weighted (T1W), T2-weighted (T2W), and diffusion-weighted (DW) contrasts. They are often acquired with gradient-recalled-echo (GRE), fast-spin-echo (FSE), balanced steady-state free procession (bSSFP), or echo-planar-imaging (EPI) pulse sequences. We implemented these imaging sequences, as well as the 3D stack-of-star (SoS) (*28*) radial sampling that is less sensitive to respiratory body motions, by careful calibration of hardware imperfections, such as field inhomogeneity and gradient eddy currents/delays. We optimized their contrasts for brain, spine, abdomen, lung, extremity, and heart using phantoms and volunteers. For each protocol, scan time was kept at 8 min or less. In general, image resolution was set to be ~2x2x8 mm^3 (~2 mm in-plane resolution and 8 mm slice thickness) by acquisition and 1x1x4 mm^3 by reconstruction for display, unless stated otherwise. Image reconstruction was performed here using traditional Fourier transform based methods, including filtered backprojection reconstruction. All protocol details for various anatomical structures and contrasts are summarized in **Table S2**. The total AC power

consumption was under 1800W while scanning for all protocols and around 300W when not scanning.

We performed 0.05 T imaging in 30 healthy volunteers (23 to 77 years old). Typical brain axial T1W, T2W, and FLAIR-like images are shown in **Fig. 2A**, delineating various brain tissues such as grey matter, white matter, and cerebrospinal fluid (CSF). They were acquired with cartesian 3D GRE, long-TR 3D FSE, and short-TR 3D FSE sequences, respectively. **Figs. 2B** and **2C** show the typical T1W and T2W C-spine and L-spine results. They were all acquired with cartesian 3D FSE sequences. Intervertebral disk and body, together with spinal cord and CSF inside spinal canal, can be identified. **Fig. S2** displays the brain and spine images from **Fig. 2** with and without EMI elimination. Deep-DSP fully removed EMI signals. Without Deep-DSP, image contents were completely obscured by EMI signals. Moreover, recently developed EMI removal methods, deep learning CNN (*12, 18*) and analytical external dynamic interference estimation and removal or EDITER (*17*), failed to effectively remove these intense EMI signals. These results demonstrated the robust ability of Deep-DSP in suppressing very strong EMI signals and enabling shielding-free 0.05 T whole-body imaging.

Figs. 3A and **3B** display the typical abdominal T1W, T2W, and DWI images. They were acquired using free-breathing 3D SoS GRE, 3D SoS FSE, and cartesian 2D EPI DWI sequences, respectively. Major abdominal structures such as the liver, large hepatic vessels, kidneys, spleen, pancreas, stomach, spine, and muscle as well as subcutaneous and visceral fat can be readily seen in these images. **Fig. 3C** shows the abdominal 3D bSSFP images. The contrast of these bSSFP images varied greatly with the flip angle, as expected, and image SNR was relatively high because the intrinsic bSSFP signal is mainly related to T2/T1 while tissue T1 relaxation times are generally much shorter at ULF (*12, 29, 30*). **Fig. 3D** displays the typical pelvis coronal T1W and T2W images from a young male volunteer, in which normal prostate substructures can be distinguished.

Fig. 4A displays the lung images. Axial bSSFP images were acquired during free breathing using 3D bSSFP sequence (with T2/T1 weighting). Free-breathing axial T2W images were

obtained with 3D SoS FSE sequence. Maximum intensity projection (MIP) images are also presented. Pulmonary vessels can be observed in the bSSFP images, while the parenchyma signal is visible in the T2W images. To demonstrate musculoskeletal imaging, the knee was scanned. **Fig. 4B**. shows the sagittal knee T1W and T2W images acquired using cartesian 3D GRE and FSE sequences. Various knee structures, such as the patella, femoral and tibial articular cartilage, and lateral and medial meniscus of the posterior horn, can be identified in these images.

Fig. 5 presents the free-breathing cardiac cine images and time-of-flight (TOF) magnetic resonance angiography (MRA) from healthy volunteers. Short-axis bright-blood cine was acquired using ECG-triggered 3D segmented bSSFP sequence from a healthy young volunteer (**Fig. 5A**). Left ventricle and myocardium can be delineated, and papillary muscle is also visible. As shown in **Movie S1**, the left and right ventricular volumes changed periodically during the cardiac cycle. The estimated volumes were derived from the middle 3 consecutive slices (**Movie S2**). The left ventricle (LV) ejection fraction was estimated to be ~60% from the LV blood cross-sectional areas, which was largely consistent with literature value (*31*). **Fig. 5B** and **Movies S3** to **S5** present the neck TOF MRA acquired using a 2D flow-compensated GRE sequence. A total of 34 slices with 4 mm thickness were obtained, covering 136 mm in the head/foot direction. With venous blood saturation, major carotid arteries can be clearly observable, including the left and right common carotid arteries, external and internal carotid arteries, as well as their bifurcations. With arterial blood saturation, major veins such as jugular veins can be readily seen.

Utilizing deep learning for enhanced image formation at 0.05 Tesla

MR signal at 0.05 T is several orders of magnitude weaker than at 3 T, the standard high-field strength, due to its proportionality to field strength squared (B_0^2) (*32*), causing high image noise and poor resolution in ULF MRI. To overcome this challenge, we turned to computing and devised deep learning-based reconstruction methods for ULF MRI image formation that are driven by the large-scale high-field MRI data (*23, 26*). We designed a partial Fourier super-resolution (PF-SR)

method that integrates image reconstruction and super-resolution (**Fig. S3**) (*26*). PF-SR model, consisting of multi-scale feature extraction, spatial attention, and reconstruction functions, was experimentally validated by comparing 0.055 T brain images to 3 T images from the same subjects (*26*). In this study, we demonstrated PF-SR reconstruction for whole-body MRI at 0.05 T. The data acquisitions typically involved 3D encoding with k-space partial Fourier sampling. See **Tables S3** to **S5** for the data acquisition, model training, and image reconstruction details. By learning the relatively homogeneous human anatomical structures and contrasts readily available in the high-field MRI datasets, PF-SR reconstruction approach advanced the whole-body 0.05 T image quality by effectively suppressing artifacts and noise, and increasing spatial resolution.

Fig. 6A and **Movies S6** and **S7** show the brain T1W and T2W images reconstructed using the conventional Fourier method (low resolution LR) and deep learning PF-SR method (superresolution SR), alongside high-resolution 3 T images obtained from a healthy volunteer. 0.05 T T1W and T2W data were acquired with isotropic 3 mm resolution using 3DFSE sequence with and without inversion recovery preparation, and scan time 5.0 and 6.2 mins, respectively. PF-SR method produced isotropic 1 mm resolution, and led to substantially improved 0.05 T image quality in terms of clarity. As confirmed by the 3 T results, numerous fine neuroanatomical structures were restored in the PF-SR images. Moreover, various brain anatomical structures appeared complementary in contrast between T1W and T2W images, as expected. **Figs. 6B** and **6C** present the typical T1W and T2W results for the C-spine and L-spine, respectively. Once again, PF-SR method enhanced the image quality, allowing improved visualization of structural details concerning the intervertebral body and disc, spinal cord, and CSF. These brain and spine results were consistent with the testing results using synthetic datasets (**Figs. S4** and **S5**, and **Movies S8** and **S9**).

Fig. 7A presents the results for abdominal imaging. With PF-SR reconstruction, various structural details, such as vessels within the liver, kidneys, stomach, pancreas, spleen, and spine, could be easily identified and delineated. Again, these anatomical structures appeared

complementary in contrast between T1W and T2W images, as expected. **Fig. 7B** and **Movie S10** show the knee images from a healthy volunteer. PF-SR enabled clearer delineation of key knee structures, including the patella, articular cartilage, and meniscus. Overall, these initial PF-SR results indicate the potential and prowess of deep learning PF-SR image reconstruction in advancing ULF MRI of various anatomical structures.

Discussion

We aim to address a critical resource challenge in healthcare - the limited and scarce access to MRI. Despite over half a century of technology development since the seminal paper published by Paul Lauterbur in 1973 (*1*), globally, clinical MRI procedures remain mostly unattainable for over two-thirds of the world's population (*6*). Historically, the development of MRI technology started at very low fields, with the earliest superconducting or resistive whole-body magnets operating at a field strength of around 0.05 T (*33, 34*). The first commercial systems, introduced in the early 1980s, reached ~0.5 T. However, the progress in low-field MRI development was halted with the introduction of the first whole-body 1.5 T superconducting scanner by General Electric in 1983 (*14*). In this study, we revisited 0.05 T whole-body MRI by reducing traditional MRI hardware requirements and harnessing computing power as well as extensive physics and engineering expertise gained over several decades. We developed a low-cost, patient-centric whole-body MRI scanner based on a permanent 0.05 T magnet that operates on a standard AC wall power outlet, without the need for RF or magnetic shielding. This scanner is compact and potentially mobile. It can be manufactured, maintained, and operated at a low cost. We experimentally demonstrated the general utility of such a shielding-free ULF scanner for imaging various human anatomical structures at whole-body level, with acceptable scan time (≤8 min per protocol) even in the presence of strong EMI. Moreover, we demonstrated the effectiveness of 3D deep learning image

formation in advancing whole-body ULF image quality by leveraging extensive high-field whole-body MRI datasets.

The whole-body ULF MRI scanner demonstrated in this study has the potential to complement existing high-performance high-field clinical MRI, especially in a point-of-care manner. By providing a more affordable and accessible option, whole-body ULF MRI can help expand the availability of MRI scans. ULF MRI offer several distinct advantages that make it an attractive option for patient comfort and safety (*12, 35-37*). These include an open scanning environment for reduced claustrophobic effect (*38, 39*), less acoustic noise during scanning for minimizing its potentially adverse effect (*12, 40, 41*), low sensitivity to metallic implants, less image susceptibility artifacts at air/tissue interfaces, and an extremely low RF specific absorption rate (SAR) (*12, 35-37*). Moreover, imaging at ULF is attractive because tissues typically exhibit dramatically shorter T1 and longer T2 and T2* at ULF (*12, 29, 30*). This enables more time-efficient data acquisition protocols due to faster longitudinal magnetization recovery and slower transverse magnetization decay, allowing for easy adaptation of SNR efficient 3D acquisitions, as shown in most protocols in this study.

Additional studies will be essential not only for advancing ULF MRI technology but also for evaluating its clinical efficacy. Recent studies by our group and others, utilizing dedicated 0.055 T and 0.064 T brain ULF MRI scanners, have demonstrated their point-of-care potential in assessing conditions such as ischemic stroke, hemorrhage, brain tumors, brain injuries, and multiple sclerosis (*12, 15, 16, 19, 42*). The present study further highlights the feasibility of imaging the C- and L-spine, another crucial central nervous system (CNS) component. Since MRI is regarded as the preferred imaging modality for the CNS due to its exceptional soft tissue contrasts (*5*), we foresee the potential application of whole-body ULF MRI in neurology clinics, trauma centers, neurosurgical suites, and neonatal/pediatric centers.

Whole-Body MRI is valuable in diagnosing and characterizing various types of cancers, such as liver, prostate, pancreatic, breast, and colorectal cancer (*43-48*). Liver cancer, for instance,

is one of the most common malignancies worldwide, with 900,000 new cases and 830,000 deaths reported in 2020 alone[55]. Hepatocellular carcinoma (HCC) is the most prevalent primary liver cancer, often diagnosed at advanced stages, resulting in poor prognosis (*49*). Recent studies have demonstrated the effectiveness of simplified MRI protocols (T1W, T2W, and DWI) for HCC screening (*50, 51*). Moreover, MRI techniques like magnetic resonance elastography and liver fat quantification have shown their efficacy in evaluating liver stiffness and steatosis, respectively, for HCC prognostication (*45, 52, 53*). In fact, these two MRI techniques can be potentially realized on our whole-body ULF MRI scanner to characterize diffuse liver diseases, despite the low SNR at ULF (*54, 55*). In addition to the CNS and abdomen, whole-body ULF MRI is valuable in assessing joints such as knee and shoulder. Additionally, cardiac late gadolinium enhancement, T1- and T2-mapping protocols are particularly effective in assessing myocardial viability and myocarditis (*56, 57*). We anticipate that that future technical development and clinical evaluation of these ULF MRI protocols will address numerous clinical needs in a point-of-care manner.

Over the past half-century, MRI has evolved from a basic concept (*1*) to an indispensable non-ionizing medical imaging modality with wide-ranging applications in diagnosing and prognosing abnormalities in the CNS, abdomen, musculoskeletal, and cardiovascular systems (*14, 27*). Owing to its soft tissue contrasts and multi-parametric nature, MRI is often preferred over other imaging modalities. Despite being regarded as one of the most notable technological advancements in modern healthcare (*3*), the overall usage of MRI ranks below CT, partly due to the greater accessibility of CT scans. Nevertheless, we argue that MRI offers the ultimate advantage of not using ionizing radiation, making it a safer option for patients. In particular, MRI is a preferred modality for repeated imaging or for vulnerable populations such as children and pregnant women. We also envision that ULF MRI can potentially play a role in image-guided biopsy or structure-sensitive treatment procedures (*58-62*), where continuous or repeated imaging is necessary.

However, advancing image quality and scan speed remains a major technical challenge for ULF MRI. The ability of ULF MRI to differentiate various soft tissues and characterize pathologies under clinical conditions is determined by the image quality and scan speed. It is crucial for ULF MRI to have adequate spatial resolution and contrast while maintaining a reasonable scan time, even in the presence of physiological motions. This is particularly important considering the availability of other imaging modalities such as ultrasound and x-ray, which are cheaper and faster. Therefore, future ULF MRI developments should encompass data acquisition~~,~~ and image formation, hardware components, and eventual clinical optimization and utilization.

Deep learning presently powers numerous advances in computational science and engineering (*20, 21*), including imaging (*63*). Deep learning will likely fuel future ULF MRI development through data-driven image reconstruction to tackle the SNR challenge. Traditional MRI data acquisition and image reconstruction methods do not rely on any prior knowledge on human anatomy, despite the relatively homogeneous and genetically predefined anatomical structures and tissue contrasts exhibited through various imaging protocols. By using such prior information through deep learning, it is plausible to boost ULF MRI quality and speed, allowing for more intelligent image formation beyond traditional Fourier or compressed sensing reconstruction. Recent studies from our group (*23, 26*) and others (*22*) have demonstrated the possibility of deep learning MRI reconstruction and super-resolution approach for brain ULF MRI by exploiting large-scale high-field brain MRI data. In this study, we have implemented and demonstrated such an image formation method, PF-SR (*26*), applied to brain, spine, liver, and knee imaging, illustrating the ability of such data-driven image formation in enhancing image resolution while suppressing noise and artifacts. Our previous studies (*23, 26*) and the preliminary brain and spine tests using synthetic datasets in this study have also shown the potential of applying this approach to datasets that contain brain and spine lesions.

However, the fidelity of the PF-SR method in restoring 3D image details remains to be carefully evaluated and optimized for each anatomical structure and contrast. As an end-to-end

supervised superresolution approach, the PF-SR image formation is prone to both blurring and structural hallucinations to a certain extent, especially in regions with fine details but low SNR and contrast (*23, 26, 64*). In fact, hallucinations can be seen among some sulci and gyri near the brain edge in the T1W PF-SR results shown in **Fig. 6A**. These hallucinations likely arose from the low SNR and poor contrast in the raw 3D ULF data. Hallucination level can increase with decreasing SNR and contrast in the input data. The effectiveness of the PF-SR method in restoring image details is limited by the interplay between noise (and unseen artifacts not accounted for during training) and predicting 3D image details using prior knowledge of specific anatomical MRI data. This prior knowledge is deeply ingrained within the PF-SR models, which are trained to learn the structural and contrast 3D multi-scale features from a large collection of standard human MR images specific to a particular organ and MRI contrast. Future research should also optimize and evaluate the capabilities of PF-SR in detecting various pathologies. To augment the PF-SR model training, we can include a diverse range of synthetic datasets that include lesions of different types, extents, and locations. This will help ensure its robustness in clinical diagnostic applications. Additionally, it may be necessary to acquire and compare both experimental ULF and high-field MRI data from the same patients to directly validate the sensitivity and specificity of the PF-SR method in detecting specific lesions. Ultimately, it is imperative to find a balance between clinical value, PF-SR output resolution and fidelity, and quality of input image data.

The extremely low SNR of MR signal at ULF continues to be a major challenge. MR signal is proportional to B_0^2, while the SNR scales approximately with $B_0^{7/4}$ at low field (*32, 37, 65*). Consequently, SNR at 0.05 T is about three orders of magnitude lower compared to 3 T. Future ULF MRI hardware development may focus on more sensitive MRI receive coils and/or more intelligent signal reception approaches at RF megahertz range via design and/or material innovation, which is a topic largely unexplored in the past development of high-field MRI. For human imaging at ULF, noise in MR signals is primarily dominated by the RF receive coil noise. Therefore, SNR can be substantially increased by cooling the RF receive coil and preamplifier, potentially through

cryogenic cooling or cryogen-free conduction cooling using cryocoolers (*66, 67*). Notably, such an approach substantially increases the coil Q factor, thus reducing the effective coil signal detection bandwidth and potentially limiting high acquisition bandwidth sequences like EPI DWI at ULF.

As a low-cost, point-of-care, and patient-friendly device, whole-body ULF MRI should operate without any enclosed RF shielding. In this study, we have successfully developed and deployed the Deep-DSP approach (*25*) that directly predicts EMI-free MR signals even in the presence of very strong EMI signals from external environments and internal electronics. Deep-DSP strategy (*25*) functions with or without dedicated EMI characterization data, considerably outperforming all existing analytical or deep learning methods that have been recently developed by our group (*12, 18*) and others (*17*). The Deep-DSP method, as illustrated in **Fig. S1**, eliminates the need for the EMI subtracting procedure utilized in CNN (*12, 18*) and EDITER (*17*) methods. This removal of the subtraction procedure mitigates the potential error propagation associated with it. The residual U-Net architecture of the Deep-DSP method is deeper and more adaptable compared to a simple CNN (*12, 18*), enabling better learning of the complex relationships between EMI signals among coils. Moreover, the Deep-DSP model, trained on synthetic data, can capture the characteristic differences between EMI signals and MR k-space signals, unlike the CNN and EDITER methods. Collectively, these factors contribute to the enhanced performance of EMI elimination achieved by the Deep-DSP method. Nonetheless, it remains imperative to continuously develop more effective methods to address complex EMI signals. Several factors contribute to this need. First, EMI signals can originate from multiple and diverse sources. Second, both MRI receive and sensing coils are unavoidably subject to baseline electronic noise, which interferes with reliably probing the electromagnetic coupling between the MRI receive coil and EMI sensing coils. Third, EMI signal propagation chain may exhibit nonlinear responses. Last, EMI source locations and/or surrounding environments may change dynamically during scanning. These largely intractable issues require further development of robust EMI elimination strategies using data-driven

approaches, especially for extremely strong and diverse EMI sources that may be encountered in unshielded whole-body imaging scenarios or in proximity to other electrical devices.

An ideal whole-body ULF MRI scanner should be lightweight and with small fringe magnetic field. Our current prototype scanner was designed primarily for conceptual demonstration without extensive hardware optimization, resulting in a relatively heavy magnet (~1300 kg) though the scanner could still be potentially mobile if equipped with a battery-operated motor system, similar to a clinical mobile CT scanner. A recent 0.2 T magnet design for brain MRI has demonstrated the possibility of reducing the double-plate magnet weight by omitting the horizontal iron poles while adding side vertical magnetic poles (*68*). With this concept and implementation of non-iron yokes, we estimate that our whole-body 0.05 T magnet weight could be substantially reduced to ~600 kg, rendering the entire scanner mobile. Future whole-body magnet development may also explore the use of low-weight homogenous cylindrical Halbach magnet designs (*9, 11*), while prioritizing a relatively large inner magnet diameter and small fringe field to ensure openness and patient comfort. Implementing such Halbach approach can greatly reduce the magnet weight and size, but it may be necessary to address the magnet thermal and structural stability issues.

In conclusion, we addressed the challenge of limited MRI accessibility by developing an affordable, simple, and computing-powered whole-body 0.05 T MRI scanner. Our low-power, compact scanner was designed to operate from a standard AC wall power outlet, without the need for RF or magnetic shielding. We demonstrated the versatility of the ULF MRI for imaging various human anatomical structures. Moreover, we demonstrated the potential of 3D deep learning reconstruction to substantially augment ULF image quality by exploiting computing power and extensive high-field MRI data. These advancements will pave the way for affordable, patient-centric, and site-agnostic MRI scanners, addressing unmet clinical needs in various healthcare settings globally.

Materials and Methods

Shielding-free whole-body MRI hardware design

The magnet design features two plates connected by four vertical pillars to optimize openness and patient comfort (**Fig. 1A**). Essential components such as the NdFeB magnet (N50), iron yoke (Q235A), pole (pure iron DT4C), silicon steel anti-eddy current plate (30ZH105), and passive shimming ring (pure iron DT4C) were developed using electromagnetic field modelling to create a uniform 0.05 T field suitable for whole-body imaging while maintaining shoulder and chest accessibility. The magnet assembly weighted ~1300 kg. While a cylindrical Halbach magnet could offer a lighter weight and smaller fringe field (*9, 11*), we chose this open double-plate design for its structural openness and patient comfort. Note that the basic structural design of this 0.05 T magnet was conceptually similar to our earlier 0.055 T magnet for brain MRI except for the iron support structure (*12*). To achieve a homogeneous field, pole pieces and shimming rings were used, along with additional passive shimming by incorporating small iron and/or NdFeB pieces, via iterative 3D field mapping and compensation. The final exterior dimensions of the magnet were 114.0 cm x 102.6 cm x 69.8 cm (width x length x height), featuring a 40 cm clear vertical gap and 92 cm width for patient entry. The final magnetic field was 0.048 T at a room temperature of 25°C, corresponding to a 2.045 MHz proton resonance frequency. The field exhibited an inhomogeneity of less than 200 ppm peak-to-peak across an oblate ellipsoid volume with a diameter of 40 cm and a height of 38 cm. The anti-eddy current plate effectively reduced overall eddy currents to below 1% in all three directions before applying any pre-emphasis compensation. The reduction made it possible to implement enabled the implement more advanced and hardware-demanding imaging sequences, such as EPI and bSSFP. The 5 Gauss fringe field was contained within 104 cm, 114 cm, and 104 cm from the magnet center in the width, length, and height directions, respectively (**Fig. 1B**). The total physical footprint of the scanner, including both the magnet assembly and electronic cabinet but excluding the detachable patient bed, was ~1.3 m^2. Note that the basic structural design

of this 0.05 T magnet was conceptually similar to our earlier 0.055 T magnet for brain MRI except for the iron support structure (*12*).

Note that the most commonly used rare earth magnet material NdFeB was chosen here over the samarium cobalt (used in recent brain ULF MRI magnet designs by our group (*12*) and commercial company Hyperfine) because it offers a higher BH_{max} of 35-50 MGOe compared to 22 MGOe for SmCo and it costs less. Despite its relatively poor temperature stability of -0.125%/°C compared to 0.015%/°C for SmCo (*69, 70*), the main magnetic field and homogeneity remained adequately stable in a standard 25°C laboratory environment (without special air conditioning) and during scanning.

Planar gradient coils, made from rectangular wire, were secured to epoxy resin boards to preserve their winding patterns. While Gx and Gy gradient coils were unshielded, Gz coil was actively shielded. Gx, Gy, and Gz coils had resistances of 83.2 mΩ, 84.5 mΩ, and 130.8 mΩ, and inductances of 280.3 μH, 254.8 μH, and 232.2 μH, respectively. Their sensitivities were 12.5 mT/m/100A, 13.0 mT/m/100A, and 6.3 mT/m/100A, respectively. A PCI GA150 switching amplifier (Performance Control Inc.), with a peak current of 150 A and a peak voltage of 150V, was used to drive the gradient coils.

Planar RF coil served as a separate transmit coil with Q factor of ~13 and ~14 when loaded and unloaded, respectively. A number of RF receive coils were constructed using the standard solenoid design (*65, 71*), including three single-channel solenoid coils for brain imaging (*12*) (200 mm by 229 mm; 8 winding turns with loaded Q of ~38), c-spine imaging (204 mm by 220 mm; 8 winding turns with loaded Q of ~49), chest and abdominal imaging (280 mm by 350 mm; 10 winding turns with loaded Q of ~37). A decoupling circuit was also implemented to detune the receive coil during RF transmission. MR signal was passed through a two-stage preamplifier module (~20 dB each). Note that, at 0.05 T, RF transmit coil was typically driven by very low RF power. For example, the non-selective 1 ms 90° block pulse only required ~100 W peak RF power, incurring negligible SAR as expected (*12, 35-37*). Gradient/RF subsystems and data acquisition

were controlled by a PC-based multi-channel NMR spectrometer console (EVO Spectrometer; www.mrsolutions.com).

Deep learning EMI Elimination by Deep-DSP

We utilized a deep learning method, Deep-DSP, developed by our group for mobile brain MRI scanners (*25*). Ten small EMI sensing coils (LC-resonant loops with 5 cm diameter) were placed near the patient bed and magnet and inside the electronic cabinet close to the gradient amplifier and console.

Deep-DSP was designed to predict EMI-free MR signals directly from the signals simultaneously detected by the MRI receive coil and EMI sensing coils (**Fig. 1C** and **Fig. S1**). During scanning, the MRI receive coil and EMI sensing coils simultaneously sampled data within two windows: one for MR signal acquisition and the other for EMI signal characterization acquisition. A residual U-Net model was then trained using synthetic MRI receive coil data and EMI sensing coil data obtained during the EMI signal characterization window (*25*). Note that the synthetic MRI receive coil data here were formed by adding the experimental EMI signals (from MRI receive coil during EMI characterization window) to a set of EMI-free brain 3 T k-space data that were arbitrarily chosen (*25*) (**Fig. S1**). Once trained, the model was used to directly predict EMI-free MR signals from the signals simultaneously collected by the MRI receive and sensing coils during the MR signal acquisition window. The U-Net model, trained using the Adam optimizer (*72*), minimized L1 loss with parameters such as batch size 64, learning rate 0.0002, $\beta 1$ 0.9, and $\beta 2$ 0.999 for 40 epochs. The average training time was ~3 min per imaging protocol on an Nvidia A100 GPU with PyTorch 2.0.1 and CUDA 11.8 on Ubuntu 22.04, which could be further shortened through both training and code optimization.

Note that, in Deep-DSP, the EMI signal characterization window was not strictly necessary. In this study, the EMI signal characterization window was specifically implemented for the 3D FSE and 2D EPI DWI sequences. To maintain the minimal TR, the EMI signal characterization

window was not implemented for all other sequences. Instead, the outer 50% k-space data collected during the MR signal acquisition window served as an alternative EMI characterization data for training the model, exhibiting no noticeable performance degradation.

ULF MRI scan protocols and optimization

Several most commonly used imaging sequences were implemented and optimized, including cartesian 3D FSE/GRE/bSSFP, cartesian 2D EPI-based DWI, and 3D SoS FSE and GRE with golden-angle radial sampling. All protocols were free-breathing. For cardiac imaging, cartesian 3D bSSFP sequence was ECG-triggered using a peripheral finger pulse oximeter. We implemented T1-weighted, T2-weighted, FLAIR-like (*12*), and DW contrasts that are most common for clinical high-field MRI. For brain and abdominal DWI, both EPI Nyquist ghosts and field inhomogeneity related geometric distortions were corrected when reconstructing b0 ($b = 0$) and b1 images (with $b \neq 0$ in s/mm^2) (*12*). Non-contrast Neck TOF MRA used a 2D GRE sequence with 1^{st}-order flow compensation in both slice selection and frequency encoding directions, with or without venous or arterial saturation. All images were reconstructed to higher display resolution by zero padding in k-space. Reconstruction was performed with standard Fourier transform together with iterative projection onto convex sets (POCSs) (*26, 73*) for partial Fourier sampling whenever applicable, except for 3D SoS radial sampling where filtered backprojection reconstruction was used. Image denoising was typically performed after image reconstruction using the standard block matching with 4D filtering (BM4D) (*74*). For cardiac cine analysis, left and right ventricles were segmented in a semi-automatic manner using Segment CMR software (https://medviso.com/cmr/). The left ventricle ejection fraction was computed by (ESV/EDV)x100%, where ESV and EDV refer to the left ventricular volume at end-systole and end-diastole, respectively, which were estimated from the middle three consecutive short-axis slices. The data acquisition and image reconstruction details for various anatomical regions (brain, C-spine, L-spine, abdomen, pelvis, lung, knee, heart, and neck MRA) can be found in **Table S2**.

Deep learning 3D PF-SR image reconstruction

PF-SR, a deep learning reconstruction method developed by us (*26*), was applied to imaging of the brain, spine, abdomen, and knee on the 0.05 T whole-body MRI scanner. PF-SR method first acquired a 3D k-space dataset using incomplete or partial Fourier sampling in k-space, then a low-resolution 3D image dataset (as input dataset) was formed by simple 3D Fourier transform. Following this, a high-resolution 3D image dataset was reconstructed using a fully 3D, end-to-end, image-domain deep learning model. This PF-SR model was specifically optimized, trained and validated for specific anatomical structure and image contrast, utilizing synthetic 3D ULF data that were simulated from the corresponding large-scale high-resolution high-field (1.5 T or 3 T) MRI data.

The overall PF-SR model architecture is illustrated in **Fig. S3** In brief, the model applied multi-scale feature extraction with a residual group (RG) inspired by the residual channel attention network (*75*) and a modified residual channel attention block for extracting multi-scale high-level features (*23*). Small kernel sizes at the top scale level enabled local image feature extraction, while an increased receptive field of 3D convolution layers at middle to bottom scale levels facilitated semi-global image feature learning (*76-78*). Channel and spatial attentions were utilized to modulate high-level features based on their inter-channel and inter-spatial relationships (*79*). The modulated features were then fed into a cascade of RGs, up-sampled to a high-resolution feature space using a 3D sub-pixel convolution layer, and transformed into a high-resolution 3D image residue using a 3D convolution layer (*23*). The final high-resolution 3D image output was generated by combining the image residue and trilinearly up-sampled model input. The PF-sampled low-resolution noisy 3D T1W and T2W ULF data were synthesized as described in the recent PF-SR study (*26*) from the corresponding high-resolution high-field data (*80-82*) (see details in **Tables S3** and **S4**). They were used for model training, validation, and testing. Each model typically

contained approximately 30 million learnable parameters, and took 2 to 8 h to train using four Nvidia A100 GPUs.

This 3D superresolution strategy, initially demonstrated for a factor of x2 with isotropic resolution in both model input and output (*23, 26*), is also applicable to non-isotropic resolution and superresolution factors at x2 or x3. In this study, T1W and T2W models were trained for brain, C-spine, L-spine, abdomen, and knee imaging and applied to corresponding datasets acquired experimentally on the 0.05 T whole-body scanner. The PF-SR models were obtained using the same model architecture and training procedure. The learning rate was adjusted based on the size of the training data. To evaluate the models, we tested them using synthetic ULF data generated from high-resolution high-field MRI data. Additionally, we compared our PF-SF method to a traditional non-deep learning method (non-DL), which involved using 2D iterative projection onto convex sets (POCS) (*83*) for PF reconstruction, followed by BM4D denoising (*74*) and tricubic interpolation. We conducted a quantitative evaluation by calculating the 3D structural similarity index measure (SSIM) (*84*) and the normalized root mean square error (NRMSE). **Tables S3** and **S4** summarize the raw data acquisition parameters, sources, and sizes of large-scale high-field MRI data used for model training, training times, and superresolution parameters. Note that only 0.05 T brain T1W and T2W data were acquired with 3 mm x 3 mm x 3 mm isotropic acquisition resolution to produce 1 mm^3 isotropic synthetic image resolution with x3 superresolution factor. All other data acquisitions remained the same as described in **Table S2**. The acquisition parameters for high-field MRI datasets (for synthesizing PF-SR training data) are summarized in **Table S4**.

Study participants

A total of 30 healthy volunteers (23 to 77 years old) were recruited for 0.05 T MRI scanning of various anatomical structures with different contrasts. Some of these volunteers were also involved during the initial protocol optimization tasks. Written informed consent was obtained from all participants before each scan, with approval from Institutional Review Board of the University of

Hong Kong/Hospital Authority Hong Kong West Cluster. To directly evaluate brain T1W and T2W PF-SR results from 0.05 T, some volunteers were also scanned using a clinical GE 3 T MRI scanner (Signa Premier) with protocol details listed in **Table S5**. A simple rigid 3D co-registration (FSL version 6.0.4) with 3D translations and rotations was performed on the 3 T brain image data to match the orientations of the 0.05 T brain image data, allowing for convenient visual comparison in **Fig. 6A**. Note the image distortions due to imaging gradient nonlinearities were not calibrated and corrected on our 0.05 T whole-body scanner.

References and Notes

1. P. C. Lauterbur, Image Formation by Induced Local Interactions - Examples Employing Nuclear Magnetic-Resonance. *Nature* **242**, 190-191 (1973).
2. P. Mansfield, A. A. Maudsley, Medical Imaging by Nmr. *Brit J Radiol* **50**, 188-194 (1977).
3. V. R. Fuchs, H. C. Sox, Jr., Physicians' views of the relative importance of thirty medical innovations. *Health Aff (Millwood)* **20**, 30-42 (2001).
4. "Magnetic resonance imaging (MRI) exams (indicator)," (OECD, 2021).
5. R. R. Edelman, S. Warach, Magnetic resonance imaging (1). *N Engl J Med* **328**, 708-716 (1993).
6. "Magnetic resonance imaging (MRI) units (indicator)," (OECD, 2022).
7. A. Webb, J. Obungoloch, Five steps to make MRI scanners more affordable to the world. *Nature* **615**, 391-393 (2023).
8. M. Naddaf, One MRI for 4.7 million people: the battle to treat Syria's earthquake survivors. *Nature* **615**, 193-194 (2023).
9. C. Z. Cooley *et al.*, A portable scanner for magnetic resonance imaging of the brain. *Nat Biomed Eng* **5**, 229-239 (2021).
10. Y. He *et al.*, Use of 2.1 MHz MRI scanner for brain imaging and its preliminary results in stroke. *J Magn Reson* **319**, 106829 (2020).
11. T. O'Reilly, W. M. Teeuwisse, D. de Gans, K. Koolstra, A. G. Webb, In vivo 3D brain and extremity MRI at 50 mT using a permanent magnet Halbach array. *Magn Reson Med* **85**, 495-505 (2021).
12. Y. Liu *et al.*, A low-cost and shielding-free ultra-low-field brain MRI scanner. *Nat Commun* **12**, 7238 (2021).
13. W. T. Kimberly *et al.*, Brain imaging with portable low-field MRI. *Nature Reviews Bioengineering*, 1-14 (2023).
14. J. Hennig, An evolution of low-field strength MRI. *Magnetic Resonance Materials in Physics, Biology and Medicine*, 1-12 (2023).
15. M. H. Mazurek *et al.*, Portable, bedside, low-field magnetic resonance imaging for evaluation of intracerebral hemorrhage. *Nat Commun* **12**, 5119 (2021).
16. M. M. Yuen *et al.*, Portable, low-field magnetic resonance imaging enables highly accessible and dynamic bedside evaluation of ischemic stroke. *Sci Adv* **8**, eabm3952 (2022).
17. S. A. Srinivas *et al.*, External Dynamic InTerference Estimation and Removal (EDITER) for low field MRI. *Magn Reson Med* **87**, 614-628 (2022).
18. Y. Zhao, L. Xiao, Y. Liu, A. T. Leong, E. X. Wu, Electromagnetic interference elimination via active sensing and deep learning prediction for radiofrequency shielding-free MRI. *NMR Biomed*, e4956 (2023).
19. K. N. Sheth *et al.*, Assessment of Brain Injury Using Portable, Low-Field Magnetic Resonance Imaging at the Bedside of Critically Ill Patients. *JAMA Neurol* **78**, 41-47 (2020).
20. Y. LeCun, Y. Bengio, G. Hinton, Deep learning. *Nature* **521**, 436-444 (2015).
21. E. J. Topol, As artificial intelligence goes multimodal, medical applications multiply. *Science* **381**, adk6139 (2023).
22. J. E. Iglesias *et al.*, Quantitative Brain Morphometry of Portable Low-Field-Strength MRI Using Super-Resolution Machine Learning. *Radiology* **306**, e220522 (2023).
23. V. Lau *et al.*, Pushing the limits of low-cost ultra-low-field MRI by dual-acquisition deep learning 3D superresolution. *Magn Reson Med* **90**, 400-416 (2023).
24. T. Guallart-Naval *et al.*, Portable magnetic resonance imaging of patients indoors, outdoors and at home. *Sci Rep* **12**, 13147 (2022).
25. Y. Zhao, L. Xiao, J. Hu, E. X. Wu, Robust EMI elimination for RF shielding-free MRI through deep learning direct MR signal prediction. *Magn Reson Med*, doi: 10.1002/mrm.30046 (2024).

26. C. Man *et al.*, Deep learning enabled fast 3D brain MRI at 0.055 tesla. *Sci Adv* **9**, eadi9327 (2023).
27. P. Bornert, D. G. Norris, A half-century of innovation in technology-preparing MRI for the 21st century. *Br J Radiol* **93**, 20200113 (2020).
28. L. Feng *et al.*, Golden-angle radial sparse parallel MRI: combination of compressed sensing, parallel imaging, and golden-angle radial sampling for fast and flexible dynamic volumetric MRI. *Magn Reson Med* **72**, 707-717 (2014).
29. P. A. Bottomley, T. H. Foster, R. E. Argersinger, L. M. Pfeifer, A review of normal tissue hydrogen NMR relaxation times and relaxation mechanisms from 1-100 MHz: dependence on tissue type, NMR frequency, temperature, species, excision, and age. *Med Phys* **11**, 425-448 (1984).
30. T. O'Reilly, A. G. Webb, In vivo T(1) and T(2) relaxation time maps of brain tissue, skeletal muscle, and lipid measured in healthy volunteers at 50 mT. *Magn Reson Med* **87**, 884-895 (2022).
31. N. Kawel-Boehm *et al.*, Reference ranges ("normal values") for cardiovascular magnetic resonance (CMR) in adults and children: 2020 update. *J Cardiovasc Magn Reson* **22**, 87 (2020).
32. D. I. Hoult, R. Richards, The signal-to-noise ratio of the nuclear magnetic resonance experiment. *Journal of Magnetic Resonance (1969)* **24**, 71-85 (1976).
33. R. Damadian, M. Goldsmith, L. Minkoff, NMR in cancer: XVI. FONAR image of the live human body. *Physiol Chem Phys* **9**, 97-100, 108 (1977).
34. W. A. Edelstein, J. M. Hutchison, G. Johnson, T. Redpath, Spin warp NMR imaging and applications to human whole-body imaging. *Phys Med Biol* **25**, 751-756 (1980).
35. J. P. Marques, F. F. J. Simonis, A. G. Webb, Low-field MRI: An MR physics perspective. *J Magn Reson Imaging* **49**, 1528-1542 (2019).
36. L. L. Wald, P. C. McDaniel, T. Witzel, J. P. Stockmann, C. Z. Cooley, Low-cost and portable MRI. *J Magn Reson Imaging* **52**, 686-696 (2020).
37. M. Sarracanie, N. Salameh, Low-Field MRI: How Low Can We Go? A Fresh View on an Old Debate. *Front Phys-Lausanne* **8**, (2020).
38. M. Dewey, T. Schink, C. F. Dewey, Claustrophobia during magnetic resonance imaging: cohort study in over 55,000 patients. *J Magn Reson Imaging* **26**, 1322-1327 (2007).
39. D. M. Hudson, C. Heales, R. Meertens, Review of claustrophobia incidence in MRI: A service evaluation of current rates across a multi-centre service. *Radiography (Lond)* **28**, 780-787 (2022).
40. C. Jin *et al.*, Temporary Hearing Threshold Shift in Healthy Volunteers with Hearing Protection Caused by Acoustic Noise Exposure during 3-T Multisequence MR Neuroimaging. *Radiology* **286**, 602-608 (2018).
41. M. J. McJury, Acoustic Noise and Magnetic Resonance Imaging: A Narrative/Descriptive Review. *J Magn Reson Imaging* **55**, 337-346 (2022).
42. T. C. Arnold *et al.*, Sensitivity of portable low-field magnetic resonance imaging for multiple sclerosis lesions. *Neuroimage Clin* **35**, 103101 (2022).
43. R. R. Edelman, S. Warach, Magnetic resonance imaging (2). *N Engl J Med* **328**, 785-791 (1993).
44. R. N. Low, Abdominal MRI advances in the detection of liver tumours and characterisation. *Lancet Oncol* **8**, 525-535 (2007).
45. W. A. Curtis *et al.*, Quantitative MRI of Diffuse Liver Disease: Current Applications and Future Directions. *Radiology* **290**, 23-30 (2019).
46. A. Stabile *et al.*, Multiparametric MRI for prostate cancer diagnosis: current status and future directions. *Nat Rev Urol* **17**, 41-61 (2020).
47. T. Kamisawa, L. D. Wood, T. Itoi, K. Takaori, Pancreatic cancer. *Lancet* **388**, 73-85 (2016).

48. K. A. Harrington, A. Shukla-Dave, R. Paudyal, R. K. G. Do, MRI of the Pancreas. *J Magn Reson Imaging* **53**, 347-359 (2021).
49. J. M. Llovet *et al.*, Hepatocellular carcinoma. *Nat Rev Dis Primers* **7**, 6 (2021).
50. P. Gupta *et al.*, Abbreviated MRI for hepatocellular carcinoma screening: A systematic review and meta-analysis. *J Hepatol* **75**, 108-119 (2021).
51. R. Girardet *et al.*, The combination of non-contrast abbreviated MRI and alpha foetoprotein has high performance for hepatocellular carcinoma screening. *Eur Radiol* **33**, 6929-6938 (2023).
52. J. Chen *et al.*, Early detection of nonalcoholic steatohepatitis in patients with nonalcoholic fatty liver disease by using MR elastography. *Radiology* **259**, 749-756 (2011).
53. R. Loomba *et al.*, Magnetic resonance elastography predicts advanced fibrosis in patients with nonalcoholic fatty liver disease: a prospective study. *Hepatology* **60**, 1920-1928 (2014).
54. M. Yushchenko, M. Sarracanie, N. Salameh, Fast acquisition of propagating waves in humans with low-field MRI: Toward accessible MR elastography. *Sci Adv* **8**, eabo5739 (2022).
55. A. Bashyam *et al.*, A portable single-sided magnetic-resonance sensor for the grading of liver steatosis and fibrosis. *Nat Biomed Eng* **5**, 240-251 (2021).
56. K. Shan, G. Constantine, M. Sivananthan, S. D. Flamm, Role of cardiac magnetic resonance imaging in the assessment of myocardial viability. *Circulation* **109**, 1328-1334 (2004).
57. M. P. Gannon, E. Schaub, C. L. Grines, S. G. Saba, State of the art: Evaluation and prognostication of myocarditis using cardiac MRI. *J Magn Reson Imaging* **49**, e122-e131 (2019).
58. J. S. Witt, S. A. Rosenberg, M. F. Bassetti, MRI-guided adaptive radiotherapy for liver tumours: visualising the future. *Lancet Oncol* **21**, e74-e82 (2020).
59. S. Verma *et al.*, The Current State of MR Imaging-targeted Biopsy Techniques for Detection of Prostate Cancer. *Radiology* **285**, 343-356 (2017).
60. M. Kobayashi, A. Pascual-Leone, Transcranial magnetic stimulation in neurology. *The Lancet Neurology* **2**, 145-156 (2003).
61. J. K. Krauss *et al.*, Technology of deep brain stimulation: current status and future directions. *Nature Reviews Neurology* **17**, 75-87 (2021).
62. P. J. Keall *et al.*, Integrated MRI-guided radiotherapy - opportunities and challenges. *Nat Rev Clin Oncol* **19**, 458-470 (2022).
63. B. Zhu, J. Z. Liu, S. F. Cauley, B. R. Rosen, M. S. Rosen, Image reconstruction by domain-transform manifold learning. *Nature* **555**, 487-492 (2018).
64. P. M. Johnson, Y. W. Lui, The deep route to low-field MRI with high potential. *Nature* **623**, 700-701 (2023).
65. A. M. Coffey, M. L. Truong, E. Y. Chekmenev, Low-field MRI can be more sensitive than high-field MRI. *J Magn Reson* **237**, 169-174 (2013).
66. F. Resmer, H. C. Seton, J. M. Hutchison, Cryogenic receive coil and low noise preamplifier for MRI at 0.01T. *J Magn Reson* **203**, 57-65 (2010).
67. J. D. Sánchez-Heredia *et al.*, Autonomous cryogenic RF receive coil for 13C imaging of rodents at 3 T. *Magnetic Resonance in Medicine* **84**, 497-508 (2020).
68. S. Wei *et al.*, Optimization design of a permanent magnet used for a low field (0.2 T) movable MRI system. *MAGMA* **36**, 409-418 (2023).
69. P. Campbell, in *Permanent Magnet Materials and their Application,* P. Campbell, Ed. (Cambridge University Press, Cambridge, 1994), chap. 3, pp. 57-81.
70. M. Sagawa, S. Fujimura, N. Togawa, H. Yamamoto, Y. Matsuura, New material for permanent magnets on a base of Nd and Fe (invited). *Journal of Applied Physics* **55**, 2083-2087 (1984).
71. B. Gruber, M. Froeling, T. Leiner, D. W. J. Klomp, RF coils: A practical guide for nonphysicists. *J Magn Reson Imaging* **48**, 590-604 (2018).

72. D. P. Kingma, J. Ba, Adam: A Method for Stochastic Optimization. *arXiv:1412.6980* (2015).
73. E. M. Haacke, E. D. Lindskogj, W. Lin, A fast, iterative, partial-fourier technique capable of local phase recovery. *Journal of Magnetic Resonance (1969)* **92**, 126-145 (1991).
74. M. Maggioni, V. Katkovnik, K. Egiazarian, A. Foi, Nonlocal transform-domain filter for volumetric data denoising and reconstruction. *IEEE Trans Image Process* **22**, 119-133 (2013).
75. Y. Zhang *et al.*, Image Super-Resolution Using Very Deep Residual Channel Attention Networks. *Computer Vision – ECCV*, 294-310 (2018).
76. O. Ronneberger, P. Fischer, T. Brox, "U-net: Convolutional networks for biomedical image segmentation" in *Medical Image Computing and Computer-Assisted Intervention–MICCAI 18th International Conference* (Springer, 2015), pp. 234-241.
77. Ö. Çiçek, A. Abdulkadir, S. S. Lienkamp, T. Brox, O. Ronneberger, "3D U-Net: learning dense volumetric segmentation from sparse annotation" in *Medical Image Computing and Computer-Assisted Intervention–MICCAI 19th International Conference* (Springer, 2016), pp. 424-432.
78. T.-Y. Lin *et al.*, "Feature pyramid networks for object detection" in *Proceedings of the IEEE conference on computer vision and pattern recognition* (IEEE, 2017), pp. 2117-2125.
79. S. Woo, J. Park, J.-Y. Lee, I. S. Kweon, CBAM: Convolutional Block Attention Module. *Computer Vision – ECCV*, 3-19 (2018).
80. D. C. Van Essen *et al.*, The WU-Minn Human Connectome Project: an overview. *Neuroimage* **80**, 62-79 (2013).
81. C. G. Peterfy, E. Schneider, M. Nevitt, The osteoarthritis initiative: report on the design rationale for the magnetic resonance imaging protocol for the knee. *Osteoarthritis Cartilage* **16**, 1433-1441 (2008).
82. J. Cohen-Adad *et al.*, Open-access quantitative MRI data of the spinal cord and reproducibility across participants, sites and manufacturers. *Sci Data* **8**, 219 (2021).
83. G. McGibney, M. R. Smith, S. T. Nichols, A. Crawley, Quantitative evaluation of several partial Fourier reconstruction algorithms used in MRI. *Magn Reson Med* **30**, 51-59 (1993).
84. Z. Wang, A. C. Bovik, H. R. Sheikh, E. P. Simoncelli, Image quality assessment: from error visibility to structural similarity. *IEEE transactions on image processing* **13**, 600-612 (2004).
85. Y. Zhao *et al.*, Whole-body Magnetic Resonance Imaging at 0.05 Tesla. *Zenodo*, https://doi.org/10.5281/zenodo.10612819 (2024).

Acknowledgements

We thank Drs V. Vardhanabhuti, F. Huang, G. Leung, W. Seto, L. Feng, and Y. Liu for advice and assistance; J. Zhang, J. Hu, P. Cao, L. Xiang, and Z. Yue for assistance; Miss K. Wu for writing assistance; and Drs C. Blackmore, J. Gore, P. van Zijl, J. Hennig, B. Rosen, G. Brittenham, M. Prince, Y. Wang, S. Formenti, P. Hua, P. Khong, E. Lee, M. Ng, W. Chew, L. Jiang, T. Foo, M. Rosen, T. Kimberly, K. Sheth, A. Webb, M. Lyu, F. Schick, J. Griffiths, J. Helpern, X. Zhang, H Fujita, L. Chen, G. Teng, D. Gao, J. Guo, J. Liu, H. Xu, H. Tong, J. Zhu, S. Zhu, S. Pourrahimi, L. Wald, C. Cooley, J. Alonso, M. Sarracanie, F. Knoll, Z. Liang, T. Vaughan, S. Geethanath, H. Yang, C. Hoven, and K. Chan for inspiring discussions and assistance. We thank Ms. S. Kwok for assistance in volunteer recruitment, and all volunteers who participated in this study. **Funding:** This work was supported by Hong Kong Research Grant Council (R7003-19F, HKU17112120, HKU17127121, HKU17127022, and HKU17127523) and Lam Woo Foundation to E.X.W. **Author contributions:** E.X.W. and Y.Z. contributed to or advised on conceptualization, design and development. Y.Z., Y.D., V.L., C.M., S.S., L.X., A.T.T.L., and E.X.W. contributed to the technical development of the system and calibrations, imaging protocols, data acquisition, preparation, and processing. E.X.W. and Y.Z. wrote the manuscript. All authors contributed to reviewing the manuscript. **Competing interests:** All authors declare that they have no competing interests. **Data and materials availability:** Primary data used, analyzed, and generated to support the findings of this study, as well as key technical design documents and custom PF-SR and Deep-DSP software code, can be accessed and downloaded from Zenodo (*85*).

Figure legends

Figure 1 Prototype of a low-cost, low-power and shielding-free whole-body ULF MRI scanner with homogeneous 0.05 Tesla NdFeB magnet and small 5 Gauss fringe field. (**A**) The scanner is designed to operate solely on a standard AC wall power outlet. It incorporates 10 small EMI sensing coils to actively detect EMI signal during scanning, has a compact footprint of ~1.3 m^2 (excluding the detachable patient bed), and requires neither magnetic nor RF shielding cages. (**B**) The magnet assembly includes iron yokes, pillars, NdFeB plates, poles, anti-eddy current plates, and shimming rings, with a vertical gap of 40 cm and a width of 92 cm. It has a homogeneity of <200 ppm peak-to-peak over a 40 cm diameter and 38 cm height oblate ellipsoid volume, and weights ~1300 kg. (**C**) The scanner uses active EMI sensing and a deep learning Deep-DSP method to retrospectively eliminate EMI in MR k-space data by directly predicting EMI-free MR signals. A 3D FSE sequence is illustrated with MR signal collection and EMI signal characterization windows. Following each scan, data collected during EMI characterization window, along with synthetic EMI-contaminated MR receive coil data, were used to train a Deep-DSP model. This model was subsequently applied to predict EMI-free MR data using data acquired during the MR signal acquisition window. Note that EMI signal characterization window is not always necessary because the outer k-space data collected during MR signal acquisition window may be used for training.

Figure 2 Typical brain and spine images from healthy adults produced by the shielding-free whole-body 0.05 T MRI scanner. (**A**) Axial brain T1W, T2W, FLAIR and DWI images from a healthy volunteer (23 years old; male) using 3D GRE (TR/TE/α° = 48 ms/6.6 ms/40°; resolution 2x2x8 mm^3), long-TR 3D FSE (TR/TE/ETL = 1500 ms/200 ms/21), short-TR 3D FSE (TR/TE/ETL = 500 ms/127 ms/13), and 2D EPI DWI (TR/TE = 1400 ms/104 ms), respectively. (**B**) Sagittal C-spine T1W and T2W images from a healthy volunteer (28 years old; male) using 3D FSE with TR/TE/ETL = 210 ms/76 ms/9 and 2300 ms/136 ms/25, respectively. (**C**) Coronal and sagittal L-spine images acquired using 3D FSE sequences (27 years old; male). Coronal T1W and T2W images were acquired with TR/TE/ETL = 190 ms/57 ms/7 and 1800 ms/170 ms/27, respectively. Sagittal T1W and T2W images were acquired with TR/TE/ETL = 190 ms/63 ms/7 and 1800 ms/172 ms/31, respectively. For each imaging protocol, scan time was 8 min or less. Image resolution was ~2x2x8 mm^3 by acquisition and 1x1x4 mm^3 by reconstruction for display. See **Table S2** for protocol details.

Figure 3 Typical abdominal and pelvic images from healthy adults produced by the shielding-free whole-body 0.05 T MRI scanner. (**A**) Axial abdominal T1W and T2W images from a healthy volunteer (28 years old; male) using 3D stack-of-star (SoS) GRE (TR/TE/α° = 35 ms/5 ms/70°), and 3D SoS FSE (TR/TE/ETL = 700 ms/111 ms/18), respectively. (**B**) Axial abdominal DWI image set from a healthy volunteer (27 years old; male) using 2D EPI DWI (TR/TE = 1250 ms/84 ms). Images with b = 0 and 300 s/mm^2 are shown, together with computed apparent diffusivity coefficient (ADC) map. (**C**) Axial abdominal 3D bSSFP images with varying tissue contrasts from the same volunteer as in **B** using different flip angles (α = 50°, 80°, 120° with TR = 8 ms). (**D**) Coronal pelvis T1W and T2W images from a healthy volunteer (28 years old; male) acquired using 3D FSE with TR/TE/ETL = 450 ms/55 ms/7 and 1500 ms/146 ms/23, respectively. For each imaging protocol, scan time was 8 min or less. Image resolution was ~2.3x2.3x8.0 mm^3 (~2.3 mm in-plane resolution and 8.0 mm slice thickness) for T1W, T2W, and bSSFP images, ~5.0x5.0x8.0 mm^3 for DWI images by acquisition. All images are displayed at reconstruction resolution 1x1x4 mm^3.

Figure 4 Typical 0.05 T lung and knee images from healthy adults. (**A**) Axial lung bSSFP and T2W images from a healthy volunteer (25 years old; male) using 3D bSSFP (TR/α° = 8ms/50°; resolution 2.5x2.5x8.0 mm³) and 3D SoS FSE (TR/TE/ETL = 1000ms/90ms/13; resolution 2.4x2.4x8.0 mm³), respectively. The corresponding maximum intensity projection (MIP) images from 5 consecutive slices are also shown. (**B**) Sagittal knee T1W and T2W images from a healthy volunteer (34 years old; male) using 3D GRE (TR/TE = 60 ms/6 ms/70°; resolution 1.4x1.9x7.0 mm³) and 3D FSE (TR/TE/ETL = 420 ms/45 ms/7 and 1500 ms/106 ms/17; resolution 1.9x2.0x7.0 mm³). Scan time was 8 min or less for each protocol.

Figure 5 Typical 0.05 T heart cine images and neck magnetic resonance angiography (MRA) images from healthy adults. (**A**) Short-axis bright-blood images from a healthy volunteer (21 years old; male) using ECG-triggered 3D bSSFP (TR/α° = 8 ms/70°; resolution 2.5x2.5x8.0 mm^3). Central 7 consecutive slices (with 8 mm thickness) are shown (see **Movie S1** for cine). The most central slice at 12 cardiac phases (out of the total 30) is displayed. Left ventricle (LV) and right ventricle (RV) volumes during cardiac cycle were segmented (see **Movie S2** for segmentation) and their changes were plotted. They were estimated from the blood cross-sectional areas within the middle 3 consecutive slices. (**B**) Neck TOF MRA MIP images acquired from a healthy volunteer (34 years old; male) with 2D TOF flow-compensated GRE (TR/TE/α° = 40 ms/10 ms/90°; resolution 2.0x2.0x4.0 mm^3) with no saturation, venous saturation, or arterial saturation, respectively. For each protocol, scan time was 8 min or less.

Figure 6 Demonstration of deep learning partial Fourier superresolution (PF-SR) reconstruction for 0.05 T brain and spine imaging. (**A**) Axial brain T1W and T2W images were reconstructed using both conventional 3D Fourier method and 3D deep learning partial Fourier superresolution (PF-SR) method from a healthy volunteer (34 years old; male). PF-SR reconstruction extended the original low resolution (LR) 3x3x3 mm^3 to synthetic superresolution (SR) 1x1x1 mm³. 3 T MRI images from the same volunteer are also shown for comparison. Note that, to facilitate visual comparison, 3T dataset was co-registered to 0.05 T dataset using rigid 3D translations and rotations. (**B**) Sagittal C-spine T1W and T2W images were reconstructed using Fourier method (LR) vs. PF-SR method (SR) from the healthy volunteer shown in **Fig. 2B**, with respective resolution 2.1x2.1x8.0 mm^3 and 1.0x1.0x4.0 mm³. (**C**) Sagittal L-spine T1W and T2W images were reconstructed using Fourier method (LR) vs. PF-SR method (SR) from the healthy volunteer shown in **Fig. 2C**, with respective resolution 2.2x2.3x8.0 mm^3 and 1.1x1.1x4.0 mm³. Please see **Table S3** for details on data acquisition, PF-SR model training, and reconstruction. 0.05 T brain T1W and T2W data were acquired using 3D FSE sequence with and without inversion recovery, and scan time 5.0 and 6.4 min, respectively. Scan time for each C- and L-spine protocol was 8 min or less.

Figure 7 Demonstration of deep learning PF-SR reconstruction for 0.05 T abdominal and knee imaging. (**A**) Axial abdominal T1W and T2W images reconstructed using both conventional 3D Fourier method (LR) vs. 3D PF-SR method (SR) from the healthy volunteer shown in **Fig. 3A**. PF-SR method extended the original low resolution 2.2x2.2x8.0 mm³ to synthetic superresolution 1.1x1.1x4 mm³. (**B**) Sagittal knee T2W images reconstructed using Fourier method (LR) vs. PF-SR method (SR) from the healthy volunteer in **Fig. 4B** with resolution 1.9x2.0x7.0 mm³ and 1.0x1.0x3.5 mm³, respectively. See **Table S3** for data acquisition, PF-SR model training, and reconstruction details. Scan time for each protocol was 8 min or less.

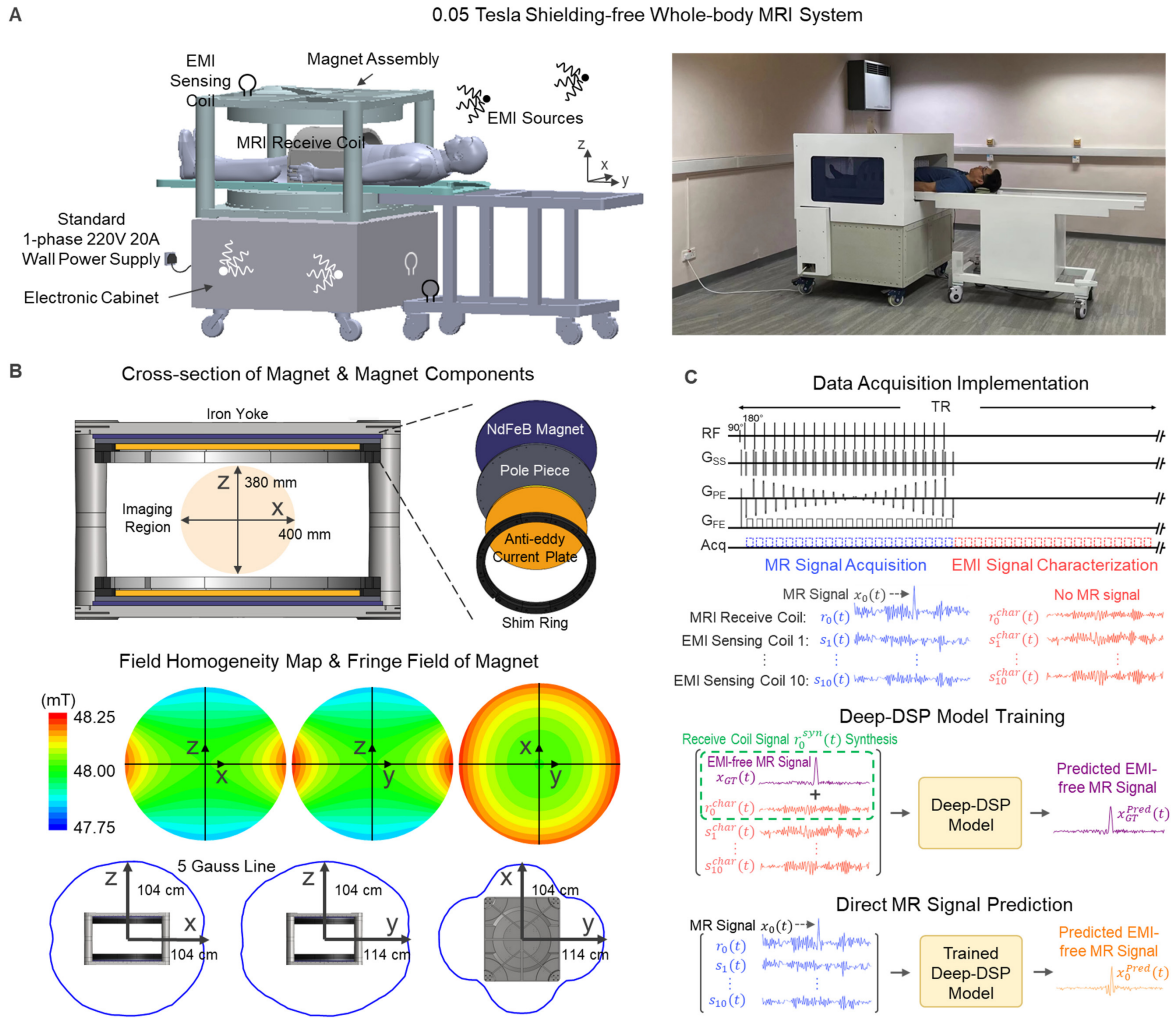

Figure 1

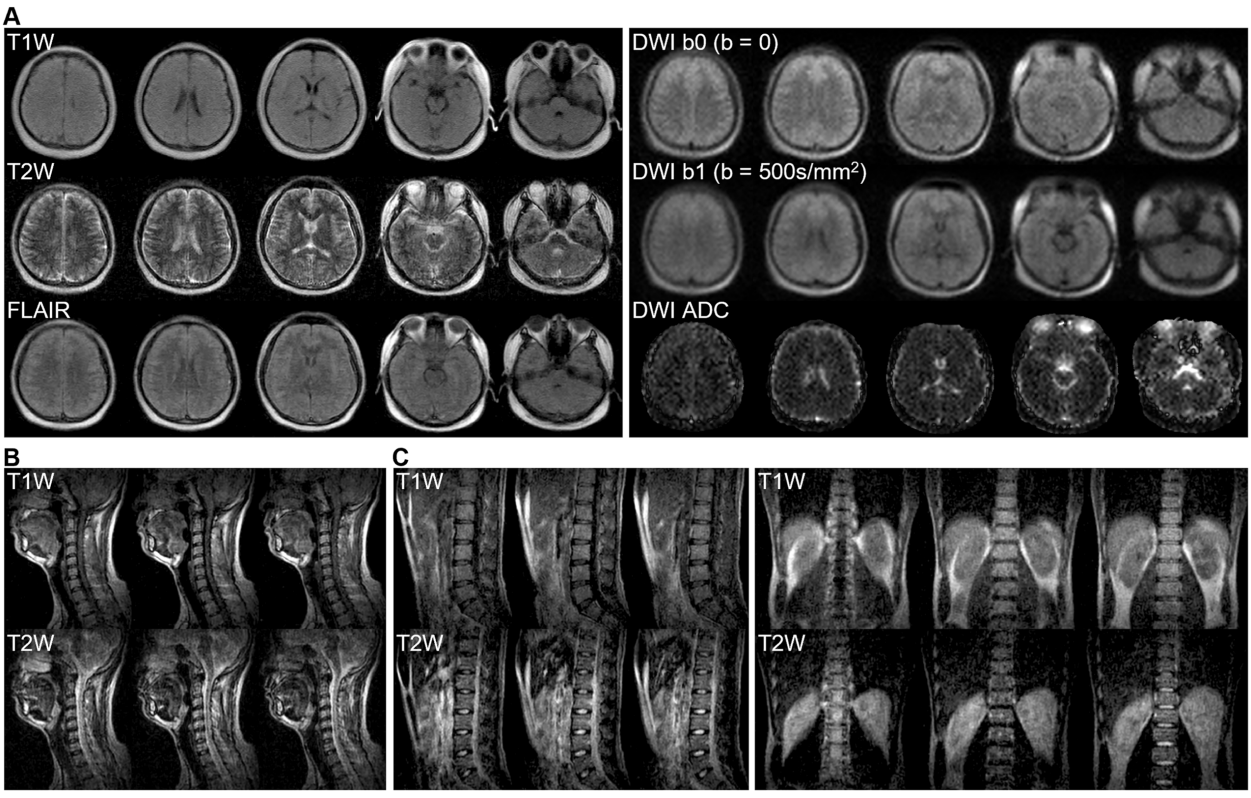

Figure 2

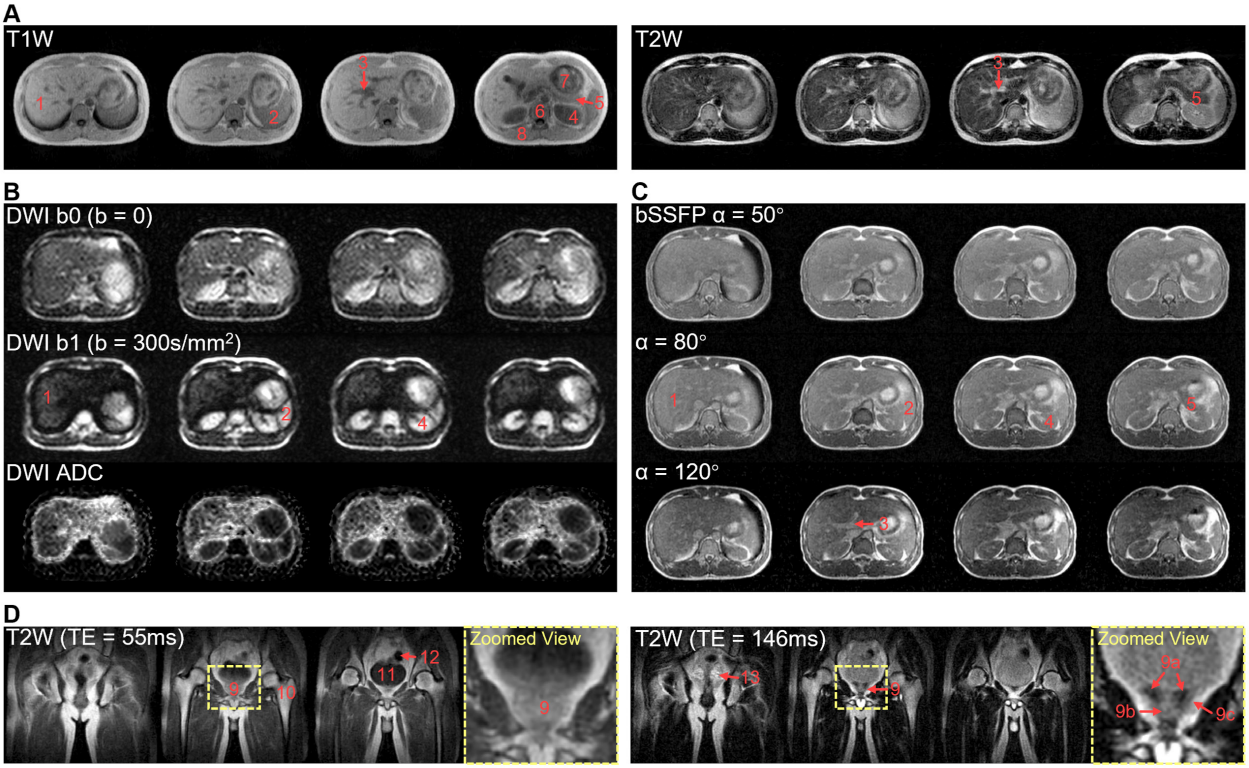

Figure 3

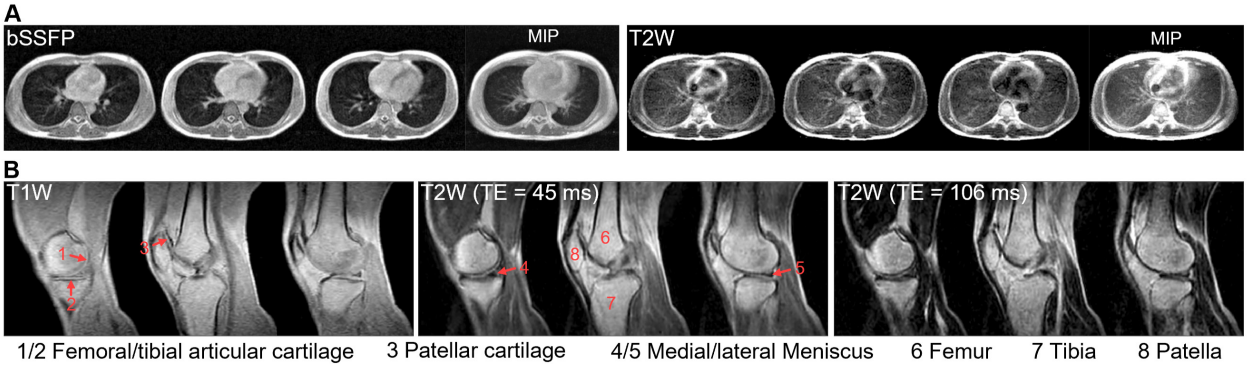

Figure 4

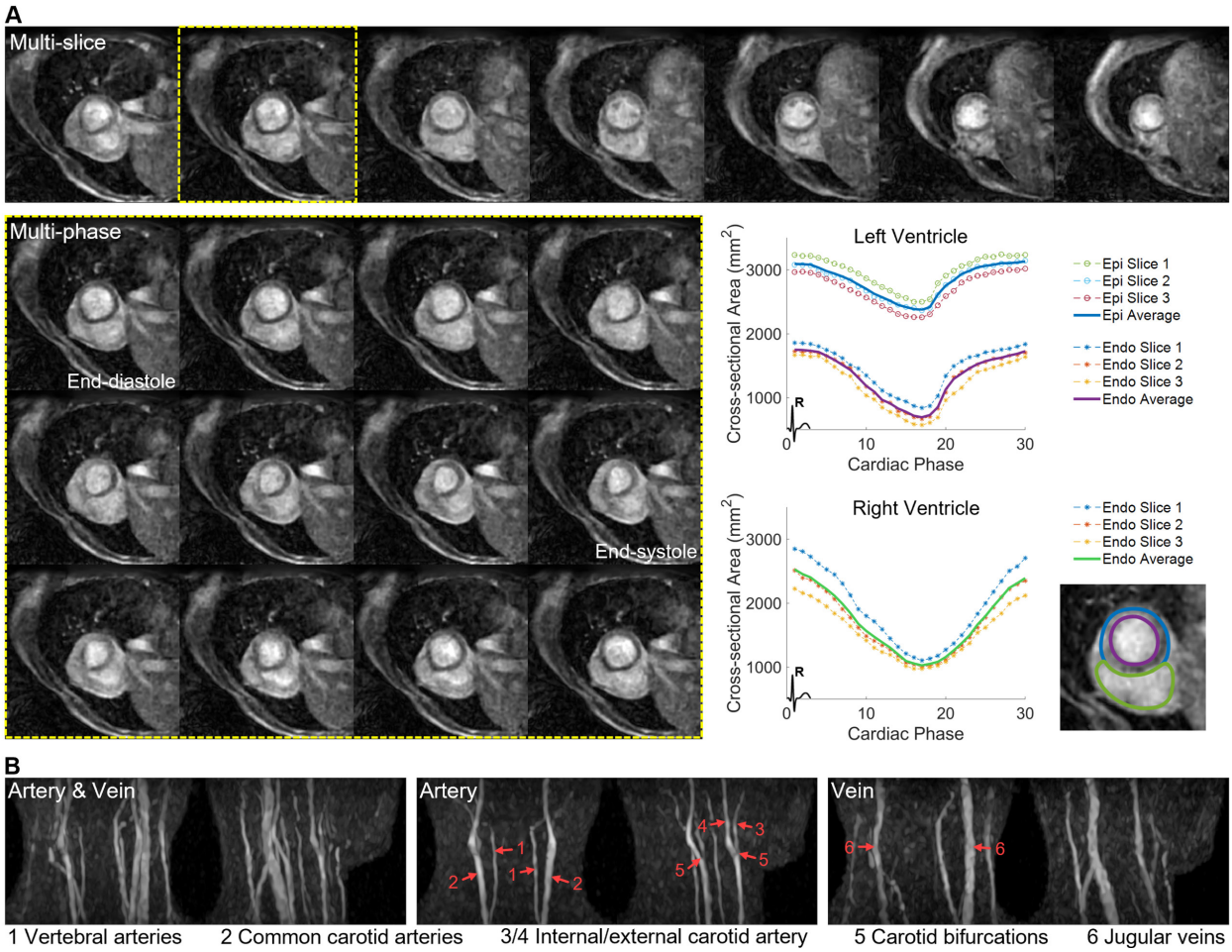
A
Multi-slice
Multi-phase
End-diastole
End-systole
Left Ventricle
Cross-sectional Area (mm²)
3000
2000
1000
0
10
20
30
Cardiac Phase
R
Epi Slice 1
Epi Slice 2
Epi Slice 3
Epi Average
Endo Slice 1
Endo Slice 2
Endo Slice 3
Endo Average
Right Ventricle
Cross-sectional Area (mm²)
3000
2000
1000
0
10
20
30
Cardiac Phase
R
Endo Slice 1
Endo Slice 2
Endo Slice 3
Endo Average
B
Artery & Vein
Artery
Vein
1
2
1
2
3
4
5
5
6
6
1 Vertebral arteries
2 Common carotid arteries
3/4 Internal/external carotid artery
5 Carotid bifurcations
6 Jugular veins

Figure 5

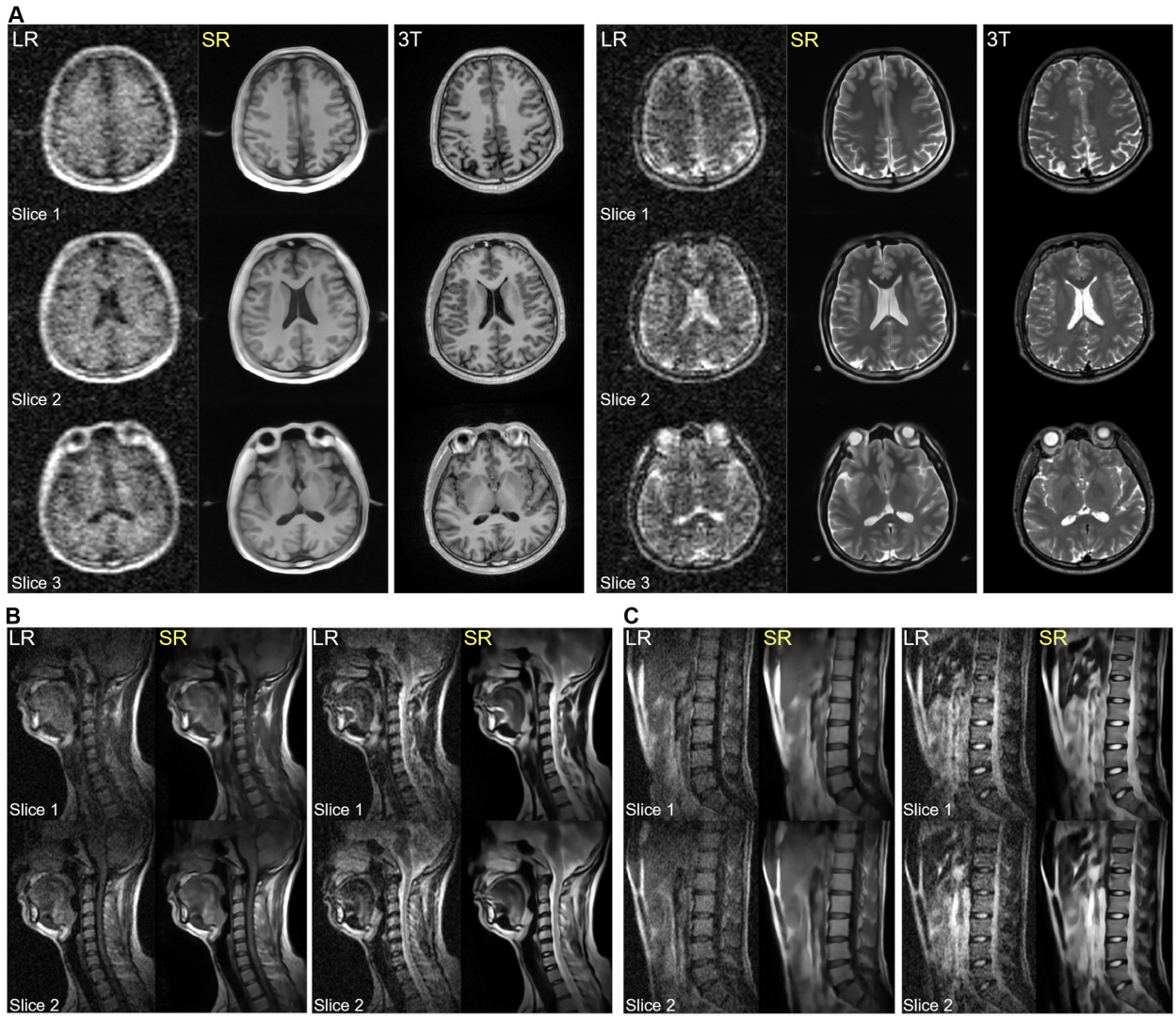

Figure 6

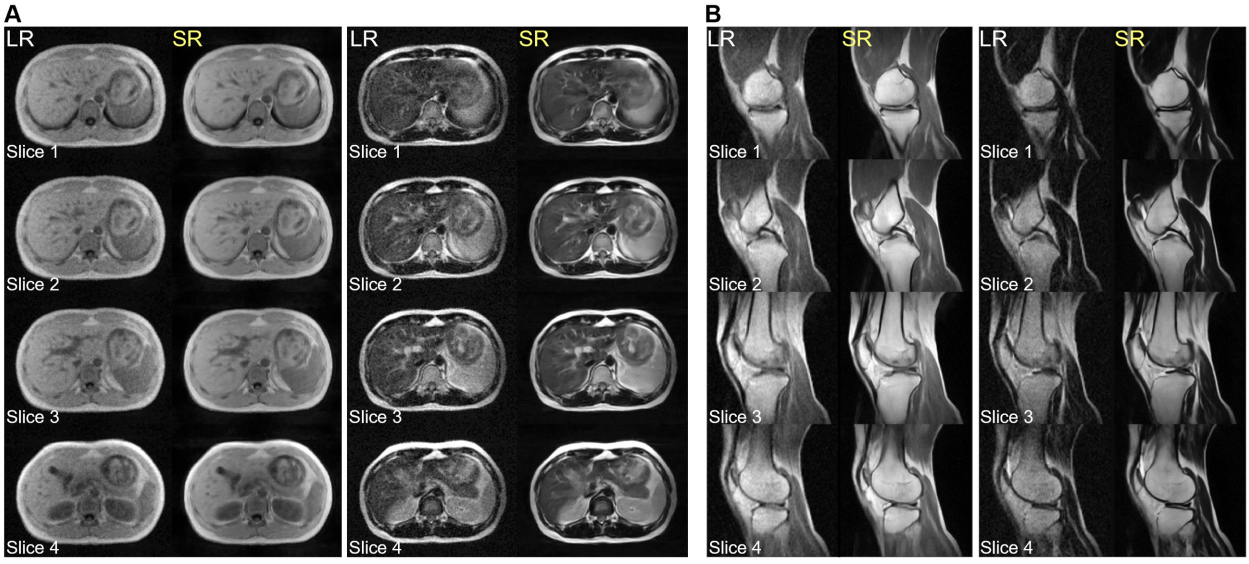

Figure 7